Research Article

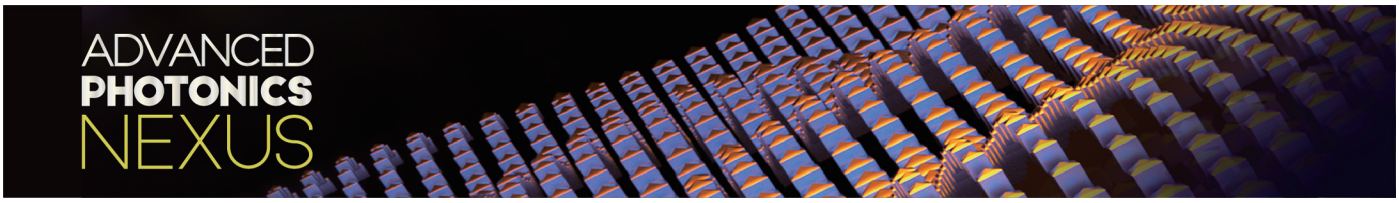

Light-sheet dynamic scattering imaging of microscopic blood flow

Kai Long,[a] Keertana Vinod Ram,[a] Shuhao Shen,[b] E Du,[c] Ziheng Ren,[d] Zhiyuan Gong,[d] and Nanguang Chen[a,e,*]

[a]National University of Singapore, Department of Biomedical Engineering, Singapore
[b]Xidian University, Guangzhou Institute of Technology, Guangzhou, China
[c]Shenzhen Institute of Information Technology, School of Microelectronics, Shenzhen, China
[d]National University of Singapore, Department of Biological Sciences, Singapore
[e]National University of Singapore (Suzhou) Research Institute, Suzhou, China

Abstract. Microcirculation imaging is crucial in understanding the function and health of various tissues and organs. However, conventional imaging methods suffer from fluorescence label dependency, lack of depth resolution, and quantification inaccuracy. Here, we report a light-sheet dynamic light-scattering imaging (LSH-DSI) system to overcome these shortcomings. LSH-DSI utilizes selected plane illumination for an optical sectioning, while a time-frequency analysis method retrieves blood flow velocity estimates from dynamic changes in the detected light intensity. We have performed imaging experiments with zebrafish embryos to obtain angiographs from the trunk and head regions. The results show that LSH-DSI can capture label-free tomographic images of microvasculature and three-dimensional quantitative maps of local blood flow velocities.

Keywords: light sheet; laser speckle imaging; flow; quantitative map; tomographic imaging.

Received Dec. 31, 2023; revised manuscript received Sep. 29, 2024; accepted for publication Nov. 7, 2024; published online Nov. 29, 2024.

[DOI: 10.1117/1.APN.4.1.016002]

1 Introduction

Microcirculation imaging is of great importance in both clinical applications and translational medical research.[1–4] It plays a crucial role in understanding the function and health of various tissues and organs for many reasons. First, the evaluation of tissue perfusion at a microvascular level provides valuable information about blood flow distribution, capillary density, and the functionality of microvessels.[5] This information is vital for assessing tissue viability, identifying areas of poor perfusion, and understanding the impact of diseases or interventions on tissue blood supply. Second, abnormal changes in microscopic blood flow patterns can be used for early detection and monitoring of various diseases, including cardiovascular disorders, diabetes, cancer, and peripheral vascular diseases.[6] Third, microcirculation imaging helps clinicians and scientists investigate the underlying mechanisms of different pathologies, such as inflammation, ischemia, angiogenesis, and microvascular dysfunction.[7] This understanding contributes to the development of targeted treatments and interventions. Fourth, microcirculation imaging techniques are valuable tools for evaluating the efficacy of various therapeutic interventions.[8] The quantitative and qualitative assessment of treatment-induced changes in microvascular parameters (e.g., blood flow, oxygenation, and vessel density) can help develop new therapies, optimize treatment strategies, and assess treatment outcomes in real time or longitudinally.[9] Finally, microcirculation imaging has the potential to contribute to personalized medicine approaches by providing essential data on individual microcirculation characteristics.[10]

Several optical methods have been established for imaging microvasculature and visualizing the flow of blood in small vessels such as capillaries. Among them, optical coherence tomography (OCT) and its functional extensions,[11] photoacoustic imaging (PAI),[12] laser Doppler flowmetry (LDF),[13–16] and laser speckle imaging (LSI)[17] are noninvasive techniques that have found a range of clinical applications. In contrast, confocal microscopy (CM) and intravital multiphoton microscopy involve the use of fluorescent dyes or intrinsic fluorescence

*Address all correspondence to Nanguang Chen, biecng@nus.edu.sg

properties of tissues to enable visualization of individual vessels, blood flow dynamics, and cellular interactions in the microcirculation.[18,19] Ultrahigh-speed OCT has been used to trace the motion of blood cell clusters in small animal models.[20] However, the most common OCT implementations for blood flow imaging are Doppler OCT or optical coherence tomography angiography (OCTA).[21,22] OCTA provides qualitative and semiquantitative information about blood flow. It does not provide absolute blood flow values or precise quantification of flow velocities and has a limited dynamic range. This limitation restricts the ability to perform precise comparisons or make absolute measurements across different cases or studies. On the other hand, Doppler OCT can provide quantitative measurements of blood flow velocities but is more susceptible to motion artifacts than OCTA.[23] PAI enables noninvasive visualization of blood flow structures and functional properties with high spatial resolution and contrast.[24,25] However, PAI has a relatively low imaging speed, which can be a disadvantage in applications where real-time monitoring of microcirculation dynamics is critical.[26,27] Compared to Doppler OCT, OCTA, and PAI, LDF and LSI are relatively inexpensive techniques, and they are easier to set up. LDF measures blood flow in microvessels by analyzing the Doppler frequency shift of laser light scattered by moving red blood cells. It provides relative blood flow measurements and is often used to assess tissue perfusion and monitor microvascular changes. LSI is a noninvasive imaging technique in which a coherent laser beam is directed onto the sample, and the resulting random speckle pattern produced by the backscattered light from moving red blood cells is captured by a camera over time.[1,3,28–39] Using correlation analysis or speckle contrast analysis to process the temporal and/or spatial fluctuations of these speckle patterns, LSI creates real-time maps of relative blood flow in the microcirculation.[4,40–48] LDF is more suitable for larger regions of interest but with a limited spatial resolution, typically in the range of millimeters. It essentially provides an integrated measurement over a relatively large area. In comparison, LSI offers a higher spatial resolution, typically in the range of tens to hundreds of micrometers. It allows for imaging of individual microvessels and provides spatial maps of blood flow distribution.

The above-mentioned conventional optical imaging methods have their advantages and disadvantages. In general, their flow assessments are qualitative or susceptible to artifacts/noises. In addition, low-cost techniques, such as LDF and LSI, have no axial resolution and cannot differentiate flow signals from different depths. We have recently combined CM with LSI to achieve tomographic flow imaging and improve quantification. However, the dynamic range and field of view (FOV) were limited.[4,40]

Here, we report a light-sheet dynamic scattering imaging (LSH-DSI) technique that can afford optimal microcirculation imaging performance in terms of tomographic imaging capability, high resolution, fast imaging rate, and quantitative flow velocity assessment. Light-sheet fluorescence microscopy is well known for its inherent optical sectioning, as it involves illuminating a thin plane of a sample with a sheet of the laser beam while capturing images typically perpendicular to the illuminated plane.[49–52] It usually offers faster imaging speeds compared to CM, as it captures an entire focal plane simultaneously. Light-sheet fluorescence microscopy has been widely used in morphological and functional imaging of zebrafish embryos, including visualization of their vasculature structures, fluid dynamics, and neuroactivities. Light-sheet platforms based on light scattering have been reported recently for structural imaging, in which the reduction and suppression of speckles are emphasized for improving the image quality.[53–55] Our technique, however, takes advantage of the dynamic changes in the scattering light to retrieve quantitative, functional parameters, such as flow velocities. LSH-DSI differs from conventional optical imaging techniques primarily in how it delivers the illumination light beam to the sample and the consequential impact on imaging quality and imaging speed. LSH-DSI utilizes a thin light sheet that selectively illuminates a thin, planar region within the sample, leading to low background noise and high imaging speed. In conventional wide-field microscopy, both the focal plane and out-of-focus regions are uniformly illuminated. It lacks optical sectioning, and the contrast tends to be low due to strong background interferences. Confocal microscopy uses point or line-scanning illumination with a spatial filter to reject out-of-focus light. However, the out-of-focus region is still exposed to the illumination light, and the imaging speed is typically insufficient for real-time imaging.

In this paper, we first present a holistically optimized optical design of a light-sheet platform for imaging microscopic flow in embryonic zebrafish models. A time-frequency analysis method is proposed for quantifying the blood flow velocities from the raw time-dependent scattering light intensity signals. The quantification accuracy is validated by comparing the LSH-DSI results with the coregistered particle imaging velocimetry (PIV) data obtained from the same trunk region of a zebrafish larva. The advantages and functionality of LSH-DSI, including its tomographic imaging capability, are further demonstrated with imaging data from the more complex head vasculature of another zebrafish larva. Our technique, in its current form, provides a simple but robust and quantitative means for three-dimensional (3D) visualization of microvessels and blood flow characteristics in suitable small animal models. Nonetheless, it is expected that it can be further developed for *in vivo* microcirculation imaging of human subjects.

2 Results

2.1 Light-sheet Dynamic Scattering Imaging System Design

We have designed and built an LSH-DSI system following the general principle of selected plane illumination but modified and optimized for functional imaging based on light scattering. As shown in Fig. 1(a), the LSH-DSI system essentially consisted of an illumination light path, a sample stage, and a detection light path. In the illumination light path, the optical output from a laser diode at 640 nm was collimated, expanded, and then condensed by a cylindrical lens (LJ1695RM-A, Thorlabs) to form an illumination light sheet after the illumination objective (123TL/05, 4×/0.1NA, Leica). Light-sheet parameters, such as its thickness and length in the focal region, were controlled by an iris aperture between the beam expander and the cylindrical lens. The sample stage had a central mounting hole for a standard glass-bottom dish on which imaging samples could be mounted. An actuator (DMX3104SH-01, NTN) is responsible for shifting the translation stage left and right for depth scanning. An optional prism attached to a glass slide was positioned underneath the sample stage, while a small air gap was maintained between the dish bottom and the top

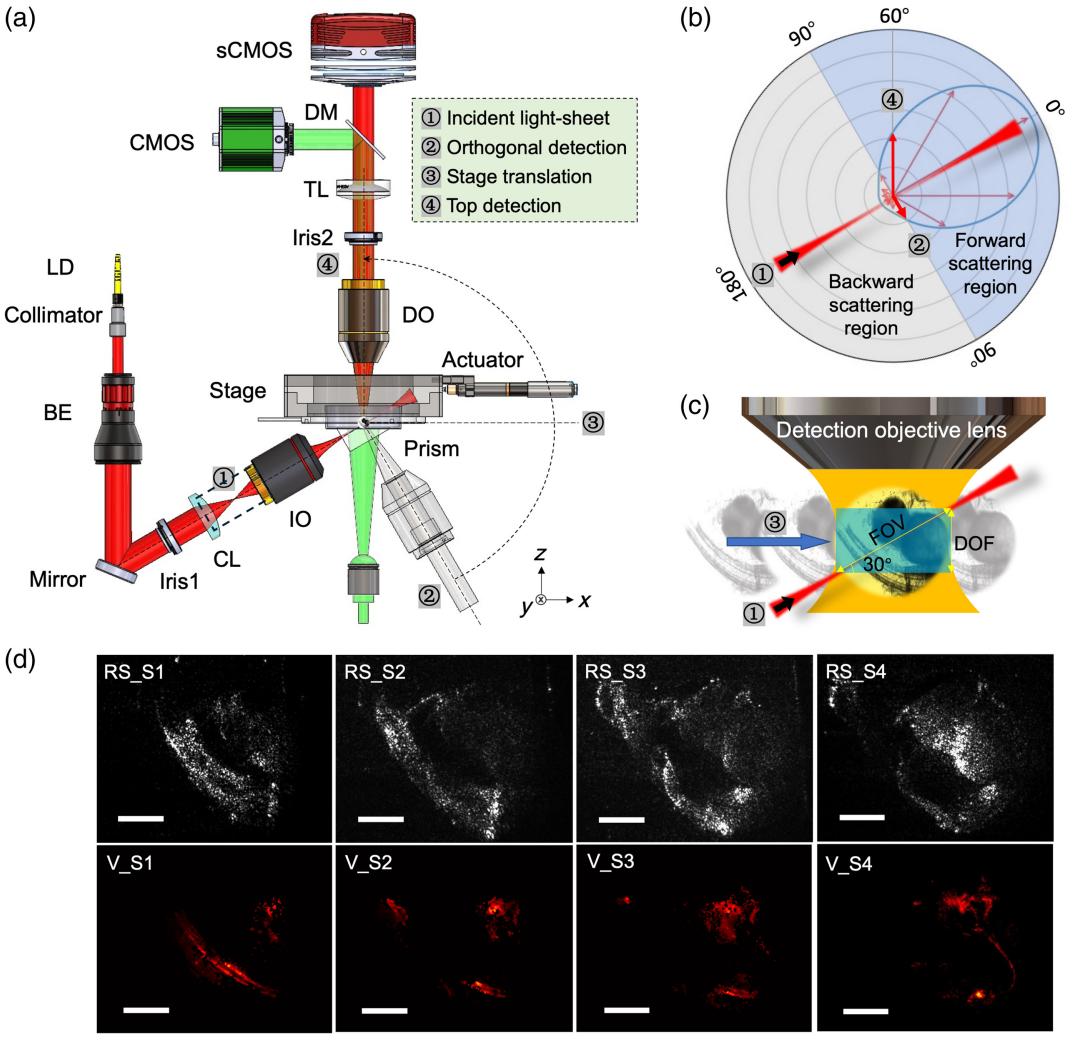

Fig. 1 Schematic of the optical setup for LSH-DSI. (a) LD, laser diode; BE, beam expander; CL, cylindrical lens ($f = 50$ mm). The dashed box after CL includes the beam view in the orthogonal plane; IO, illumination objective; TL, tube lens ($f = 100$ mm); DO, detection objective; DM, dichroic mirror. (b) Anisotropic scattering in tissue and detected signal intensity versus scattering angle. (c) Layer-by-layer scanning enabled by sample translation. (d) Example LSH-DSI images. The first row: raw speckle images; The second row: corresponding blood flow velocity maps. S1, S2, S3, and S4 denote four different slices separated by 100 μm. RS indicates raw speckle images while V represents velocity maps. Scale bars: 200 μm.

surface of the glass slide. The prism helped minimize the diffraction and aberrations of the illumination beam. The orthogonal arrangement of illumination and detection axes is the standard practice in fluorescence light-sheet microscopy. For dynamic scattering imaging, however, this orthogonal light path is suboptimal. Light scattering in biological soft tissues usually favors small scattering angles (so-called forward scattering). For example, the estimated anisotropic factor (the average cosine of scattering angle) is ~0.95 at 640 nm,[55] considering a typical size of 10 μm for red blood cells. Due to forward scattering, the detected photon intensity depends critically on the detection geometry [Fig. 1(b)]. To capture more scattering photons for improved image quality and image acquisition speed, we chose a vertical detection light path on top of the stage. Typically, the illumination light sheet formed a 30 deg angle with the horizontal stage surface, leading to a 120 deg angle with the detection optic axis. Oblique light-sheet optical implementation has been developed in recent years. Its technical advantages and design considerations have been reported in many previous studies.[56] A $10\times/0.25$NAOlympus objective lens collected forward-scattering photons with relatively small scattering angles (around 60 deg) and projected them via a tube lens onto a Scientific COMS (sCMOS) camera (pco.dimax cs1, Excelitas Technologies® Corp). The sCMOS camera could capture raw speckle images at a full-frame (1296 pixel × 1024 pixel) rate of up to 3086 frame/s (fps) and reach 10,782 fps for a moderate image size of 528 pixel × 528 pixel.

Figure 1(c) highlights a design challenge associated with the slanted illumination light sheet. In contrast to the orthogonal detection geometry, it is impossible to position the tilted light sheet within a tight depth of focus (DOF). To achieve a uniform spatial resolution, it is necessary to control the effective

numerical aperture of the detection objective (DO). We added another adjustable iris at the back of the DO for this purpose, ensuring that the DOF could adequately cover the effective length of the light sheet (see Appendix A).

The dynamic scattering imaging system is supplemented by a wide-field light microscope that can operate simultaneously during dynamic scattering image acquisition. This wide-field subsystem consisted of a green LED at a center wavelength of 520 nm for wide-field illumination, while the same DO for LSH-DSI was used to collect the transmitted photons. A dichroic mirror (DMLP605R, Thorlabs) was used to pass the red light for LSH-DSI but reflect the green light toward a general-purpose machine vision CMOS camera (UI-3060CP-M-GL Rev.2, IDS) for acquiring transmission images. The wide-field transmission microscopic images were analyzed using a PIV program (PIVlab, see Appendix A). PIV results provided complementary flow and vasculature information and a cross-validation method for dynamic scattering imaging.

To obtain a two-dimensional (2D) LSH-DSI flow map, we first positioned the light sheet in an appropriate region inside the sample. Raw images were transferred from both cameras to a PC and displayed on a monitor in real time for the operator to find regions of interest. Afterward, the operator could adjust the sCMOS frame rate and exposure time to acquire raw image sequences. A raw image sequence was typically processed with an algorithm based on spectral analysis pixel by pixel. Consequently, the local frequency shift was converted to a flow velocity and assigned to the corresponding pixel. 3D sample scanning was performed by laterally shifting the sample (and sample stage) with respect to the stationary illumination light sheet using the actuator digitally controlled via a data acquisition (DAQ) device (USB6008, National Instruments).

Figure 1(d) shows sample laser speckle images obtained from a 2-dpf zebrafish embryo. The gray-scale maps in the first row are time-averaged intensities in the raw image sequences captured at four different sample planes separated by a 100-μm interval. The image acquisition speed was 450 fps. While some morphological features were visible in the raw images, it was very challenging to identify and discern the vascular system. With autocorrelation analyses, however, we obtained high-definition blood flow maps for various parts of the embryo (displayed in the second row).

2.2 Cross-Sectional Imaging of Blood Flow in the Zebrafish Larva Trunk

The vascular structure in the trunk region of zebrafish larvae is relatively simple. It is easy to capture high-quality transmission images in which individual blood cells can be distinguished and tracked to yield reasonably reliable measurements of blood flow velocities, especially in those major vessels. Therefore, the trunk region can serve as a test site for cross-validating the LSH-DSI method with transmission-imaging-based PIV.

We acquired both dynamic light scattering and wide-field transmission imaging data from a zebrafish larva at 3 days post fertilization (dpf). As shown in Fig. 2(a), the light sheet intersected the trunk at an angle. The raw images in the trunk region were collected under the condition that the light sheet was around 54 μm in length and 4 μm in thickness (illumination NA 0.1) with a 24-μm DOF (detection NA 0.25). Major blood vessels in the trunk region [the dorsal aorta (DA) and the posterior cardinal vein (PCV)] were oriented horizontally to facilitate the acquisition of high-quality wide-field transmission images at 200 fps over 2 s. Figure 2(a) also shows a compound cross-sectional LSH-DSI angiograph of the trunk, in which the DA and PCV are indicated by a red triangle and a green arrow, respectively. An example frame of transmission image [Fig. 2(b1)] covered both DA and PCV, in which blood cells were readily distinguishable from the background. The vectorial flow maps [Figs. 2(b2) and 2(b3)] were generated by PIV analyses with PIVlab (see Appendix A). The unit for the flow velocity was pixel per frame. Local instantaneous blood flow velocities in both DA and PCV were quantitatively estimated by applying a one-dimensional PIV analysis MATLAB code to the sampling regions of 40 pixel $\times$ 20 pixel [indicated by white boxes in Fig. 2(b3)] and functioned as approximate ground truths for the comparison study.

The acquisition rate for raw LSH-DSI images was 3000 fps, and the exposure time was 20 μs, leading to a stack of 6000 frames over 2 s. They were intensity maps of light scattered from the sample cross section [Fig. 2(c)] sliced through by the light sheet. The high spatiotemporal resolution in the raw image stack afforded crucial insight into complicated dynamic signal characteristics and was very beneficial in the signal processing and interpretation. As one can see from an example scattering light signal picked from a DA pixel [Fig. 2(d)], the intensity fluctuated in a seemingly random manner. However, there was a periodic pattern in the instantaneous oscillation frequency. The periodicity was confirmed with a time-frequency analysis (see Appendix A for details), which resulted in the short-time power spectrum, as shown in Fig. 2(e). The frequency shifts were caused by the interference between detected light waves scattered from stationary tissues (e.g., vessel wall) and moving red blood cells. They can be readily converted to the local and instantaneous flow velocities. The quantification accuracy of this simple frequency-domain analysis method was validated by comparing the LSH-DSI and transmission PIV results.

The highly pulsatile arterial (DA) blood flow waveforms were plotted in Fig. 2(f). The LSH-DSI (blue line) and PIV (red line) results had very similar dynamic characteristics in terms of peak value, valley value, pulse width, and rising and falling edges. Based on a statistical analysis of the five pulses, the peak arterial flow velocity was estimated at (595.7 ± 23.1) μm/s (LSH-DSI) or (612.4 ± 30.9) μm/s (PIV). Averaging over the 2-s time window, the flow velocity was 254.3 μm/s (LSH-DSI) or 254.4 μm/s (PIV) in the DA. In the PCV, the blood flow was more stationary. Nevertheless, residual periodic changes in the flow velocity were still visible in the LSH-DSI waveform [Fig. 2(g), blue line]. The LSH-DSI estimated mean value (179.4 μm/s) was slightly higher than that of PIV (145.6 μm/s). While the relative difference appeared larger, the absolute difference was consistent with the measurement errors for both methods. These results suggest that LSH-DSI can quantitatively map local flow in terms of absolute velocities instead of relative changes afforded by conventional laser speckle contrast imaging.

2.3 3D Imaging of Blood Flow in the Zebrafish Larva Head

The blood vessel network and flow patterns are much more complicated in the head region. To further demonstrate the advantages of LSH-DSI, we collected experimental imaging data from the head of a 4-dpf zebrafish larva. Figure 3(a) shows one

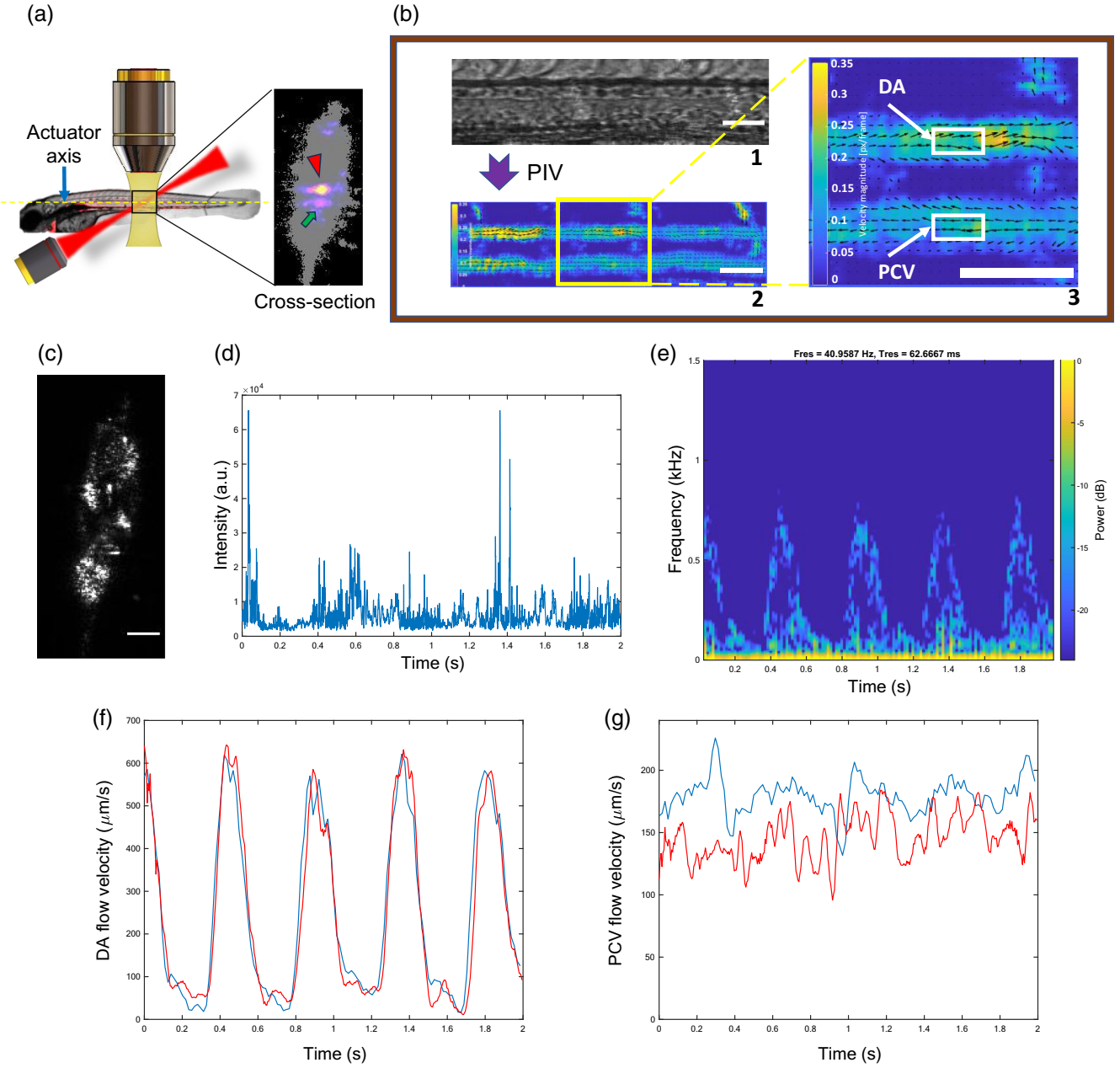

Fig. 2 Quantitative comparison of blood flow velocities measured with LSH-DSI and PIV. (a) Imaging geometry. (b) Flow mapping with PIV. 1, wide-field transmission image covering both DA and PCV; 2 and 3, PIV analysis results showing blood flow in opposite directions along the DA (up) and PCV (bottom). (c) A sample raw LSH-DSI image. (d) Representative light-intensity signal picked up from a pixel in the DA. (e) Short-time power spectrum of the signal in (d). (f) Comparison of DA blood flow velocities obtained from LSH-DSI (blue) and PIV (red). (g) Comparison of PCV blood flow velocities obtained from LSH-DSI (blue) and PIV (red). Scale bar: 50 μm.

frame of the transmission images, which is used to illustrate the LSH-DSI scanning process. The zebrafish was shifted from left to right step by step, while its head-tail central axis was oriented perpendicular to the actuator axis. Equivalently, the light sheet slicing through the head moved from right to left and the normal distance between neighboring slices was ~25 μm. The central location of the light sheet at each scanning step corresponded to one of the red dashed lines superimposed on the transmission image.

Adapting to the size of the zebrafish larval head, both the IO and DO irises were adjusted to have a light sheet around 602 μm in length, 13 μm in thickness (illumination NA 0.03), and a 393-μm DOF (detection NA 0.05). The transmission images obtained at 200 fps over 2 s were also processed by PIVlab with the same parameter settings as above to generate a 2D flow map [Fig. 3(b)].

Raw LSH-DSI images were acquired at 1500 fps (with an exposure time of 20 μs) for 2 s at each of the 15 light-sheet

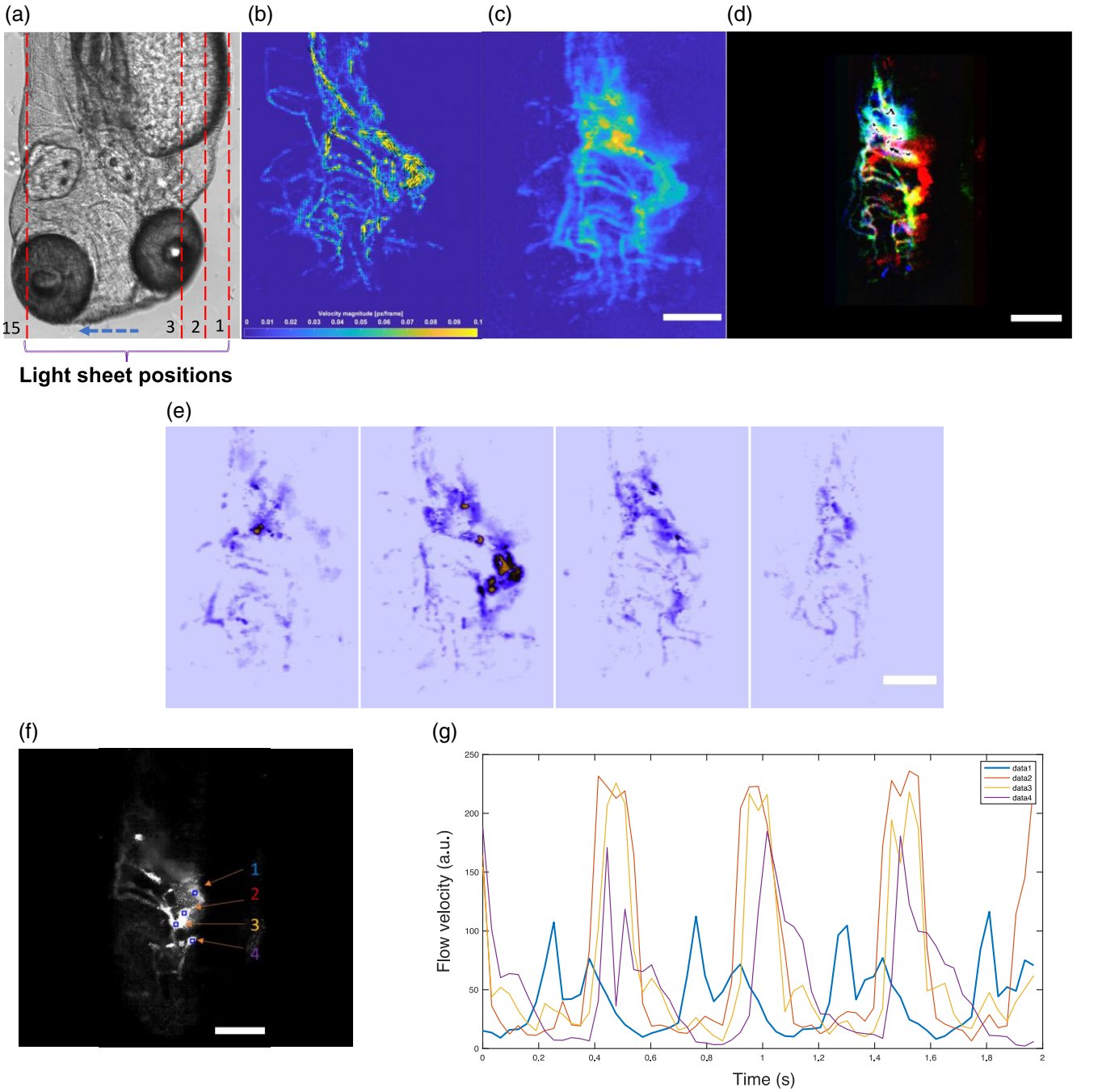

Fig. 3 Head vascular imaging. (a) A transmission image of the sample. (b) A 2D flow map generated with the PIV analysis of transmission images. (c) Simple projection of 15 LSH-DSI angiograph slices. (d) Combo LSH-DSI velocity map including three consecutive slices, which were coded in red, green, and blue colors to distinguish them. (e) Representative en face angiographs from the reconstructed image stack [Video 1 (AVI, 2.85 MB) [URL: https://doi.org/10.1117/1.APN.4.1.016002.s1]. The layer depths from the bottom were 118, 149, 188, and 228 μm, respectively. (f) Four test points were selected (marked by blue squares) on a single slice (No. 4) angiograph to estimate local blood flow velocities. (g) Blood velocity waveforms measured with LSH-DSI. The line colors matched those of testing point indices in (f). Scale bars: 200 μm.

locations. In total, the image acquisition time was ~8 min, including the time for data transfer from the camera memory to the computer (264 pixel × 476 pixel per frame, 3000 frame for each step), stage translation, and stabilization. The raw images were first processed to generate speckle contrast maps (see Note S2 in the Supplementary Material), which were simply the ratios of temporal standard deviations to mean intensities. These speckle contrast maps outlined the vasculature structures and were used to generate (binary or analog) masks of vessel regions.[41] We then further processed the raw images for each

of the 15 light-sheet slices using the same time-frequency domain analysis method as mentioned above and generated a blood flow image sequence for each slice. The flow velocity quantification was primarily performed in the vessel regions. Averaging the flow velocities over time, we obtained the slice-by-slice angiographs. The projection of all 15 angiograph slices is shown in Fig. 3(c), which demonstrates striking similarity in morphological details with Fig. 3(b), except in areas where there is vessel overlapping or complex 3D flow (e.g., in the heart region). To show the optical sectioning capability of LSH-DSI, we created a composite image [Fig. 3(d)] consisting of LSH-DSI angiographs from three neighboring slices (No. 4 to No. 6), color-coded in red, green, and blue, respectively. A significant part of the heart emerged in pure red, as it was largely captured in layer 4. Many small vessels attached to aortic arches appeared in pure green or blue. They were in layers 5 and 6 and could be well separated by LSH-DSI. Structures in composite colors (such as white, yellow, and cyan) were mostly associated with relatively big vessels (such as the common cardinal vein) or vessels running across layers. The angiographs were further processed using interpolation to generate a finer 3D stack of 300 en face images (see Video 1). The depth interval was 1 μm, while the total depth range was 300 μm. A few representative frames (rendered in the ICA color map) are displayed in Fig. 3(e). From left to right, they were positioned at 118, 149, 188, and 228 μm, respectively, from the bottom of the stack. To better visualize the 3D network of blood flow in the zebrafish larva head, a 3D rendering rotating along the y axis is provided in Video 2.

The blood flow in the heart was rather complicated. Red blood cells moved three-dimensionally, in contrast to the essentially one-dimensional flow in small vessels. Therefore, it was challenging to track individual blood cells in transmission images and obtain quantitative flow velocity measurements. On the other hand, LSH-DSI was capable of tomographic and quantitative visualization of the dynamic flow around the heart region. Four test points (marked by blue squares) were picked from an angiograph [Fig. 3(f),] and the corresponding flow velocity waveforms were plotted in Fig. 3(g). The first test point was located inside the heart. The flow velocity waveform (blue line) had two peaks in each cardiac cycle. The first peak was associated with the inflow of blood cells during the diastolic phase, while the second peak was related to the outflow in the contractile phase. The fast-rising edge of the blood flow (red line) in the dorsal aorta (DA; the second test point) almost coincided with the peak outflow from the heart. However, it reached much higher peak velocity values. For test points (No. 3 and No. 4) at downstream arteries, the small time delays in the rising edge and the gradual decrease in the peak velocity were nicely reproduced.

It is evident that LSH-DSI has significantly extended the functionality of conventional laser speckle imaging by providing 3D, layer-by-layer maps of flow velocities. Furthermore, the 3D imaging capability is achieved together with improved quantification and high temporal resolution.

3 Discussion

We have experimentally demonstrated the performance of LSH-DSI in terms of 3D imaging and dynamic flow velocity quantification. These technical advantages are a natural outcome of our novel optical design, system optimization, and appropriate flow quantification algorithm.

Light-sheet illumination is the key to optical sectioning without spatial filtering (as in confocal microscopy) or numerical postprocessing (as in structured illumination microscopy). Unlike fluorescence lightsheet microscopy, LSH-DSI is based on an intrinsic contrast mechanism (light scattering) and is a label-free imaging platform. Like fluorescence light-sheet microscopy, however, the optical sectioning capability of LSH-DSI could be compromised by inhomogeneities and scattering in tissue samples. In addition, the axial resolution must compromise with the FOV and DOF. Nevertheless, LSH-DSI provides an excellent solution to experimentally investigating fluid dynamics in sophisticated 3D networks.

The light sheet tilted with respect to the detection optic axis is another indispensable feature that helps enhance the detected signal. Compared with the backscattering light in a confocal setup, the forward-scattering signal captured in LSH-DSI is stronger by many orders of magnitude. As a result, there is great flexibility in configuring the image acquisition speed and exposure time without worrying about the photon budget. In our imaging experiments, the camera exposure time was as short as a few microseconds, while the illumination light power was <11 mW. The high-speed imaging capability is desirable for enhanced dynamic range in flow velocity measurement. However, this is not its only benefit. It also enables fast DAQ and helps improve the overall throughput, especially in 3D imaging.

Notwithstanding all the benefits of the slanted light sheet, LSH-DSI is by no means limited to this specific configuration. In the case of an adequate photon budget, the conventional orthogonal detection geometry [see Fig. 1(a)] could be a better option to allow faster depth scanning without using the translation stage. Furthermore, the illumination and detection optics can both be shifted above the sample stage to accommodate other small-animal models that are less transparent.

Model fitting has been a tricky process in laser speckle imaging, with many uncertainties. Our investigation has revealed the complicated nature of dynamic scattering signals, which requires delicate theoretical treatment. The dynamic change in the detected light intensity comprises two components. The first component is generated by the interference of light scattered from a group of scattering particles (primarily red blood cells in this study) that move independently of each other. It is random in nature. The second component, on the other hand, is more periodic and results from the interference of light scattered from stationary structures (e.g., the vessel wall) and moving scatters. We previously attempted to retrieve the decorrelation time associated with random intensity fluctuations and tried to separate them from an underlying periodic oscillation. However, the separation process was a bit tricky. It worked well for continuous flows in veins but was not so effective in dealing with dynamic flows in arteries, for which the frequency shift varied too quickly. The frequency domain analysis method presented in this paper leads to a more robust imaging processing algorithm for quantifying local flow velocities. It is especially suitable for microcirculation imaging as blood cells are moving in close proximity to microvessels. Consequently, the Doppler signals become adequately strong for accurate frequency shift estimation.

It should be noted, however, that the flow velocity estimate depends on the orientation of the vessel relative to the illumination and detection light paths. In zebrafish head vasculature imaging, the initially estimated velocities (as shown in Fig. 3)

were relative instead of absolute, as the local vessel orientations were unknown. Nevertheless, this morphological information could be recovered once the 3D angiograph was reconstructed. In principle, the local flow velocities could be consequently corrected and quantified.

We plan to investigate further in the future to improve our imaging technique from various aspects. Powerful deep-learning approaches will be leveraged to suppress noises in flow velocity maps for better visualizing slow flows, perform proper vessel segmentation, and enhance spatial resolutions (especially the depth resolution). In addition, there is room for improvement in terms of optical and mechanical designs. Our current setup relies on mechanical translation to achieve sample scanning. The use of a translation stage ultimately limits the 3D imaging speed and may lead to image distortion and motion artifacts. Therefore, it is desirable to develop and adopt a fast-scanning mechanism to shift the light sheet rapidly inside the sample. Special beam techniques (e.g., scanning Bessel beam) could be integrated into our platform to extend the FOV without compromising spatial resolutions. In terms of future applications, we are very interested in adapting our technique to visualize microcirculation in human subjects.

In conclusion, we have developed a novel laser speckle imaging system augmented by wide-field transmission imaging for cross-validation. A series of validation experiments have demonstrated the performance of LSH-DSI, including optical sectioning, outstanding flow quantification accuracy, and high spatial and temporal resolution. While LSH-DSI is an excellent platform for zebrafish embryos and larvae, it can be adapted to flow imaging for other small-animal models, such as mouse and fruit fly larvae. In addition, there is a great potential to further develop it for medical applications where 3D and quantitative label-free flow imaging is essential.

4 Appendix A: Materials and Methods

4.1 Sample Preparation

Zebrafish embryos and larvae were used as samples in our *in vivo* imaging experiments. According to NUS Institutional Animal Care and Use Committee (IACUC) guidelines, zebrafish embryos or hatched larvae in the yolk sac stage up to 5 days post-fertilization are not considered "live vertebrate animals." The research will not be subjected to IACUC review if the zebrafish embryos/larvae will be euthanized 5 days post-fertilization. In our study, the zebrafish were stored in a 28°C incubator after fertilization. In the first three days, the zebrafish larva was cultured in 0.003% PTU solution to remove melanin during development. Before imaging experiments, the zebrafish were anesthetized with 0.02% Tricaine and then immobilized with 3.5% methylcellulose in a Petri dish where the bottom was a thin coverslip.

4.2 System Configuration and Data Collection

The raw data acquisition process was one of the most important factors determining the accuracy of blood flow velocity measurement. It was critical to properly configure the laser wavelength, the light-sheet thickness, and the image acquisition speed for different samples.

The thickness and length of the light sheet were estimated from these two parameters:

$$w_0 = \frac{\lambda}{\pi NA_{IO}} \quad \text{and} \quad z_R = \frac{nw_0}{NA_{IO}}, \tag{1}$$

where n is the medium refractive index, λ is the laser wavelength, NA_{IO} is the illumination objective numerical aperture, w_0 is the Gaussian beam waist radius, and z_R is the Rayleigh range. The effective beam thickness was simply $2w_0$, while the effective beam length for even illumination was $2z_R$. A thicker light sheet was associated with a lower axial resolution but a larger usable FOV, and vice versa. The light-sheet thickness also had a strong influence on the optical sectioning capability of the system and the accuracy of the blood velocity quantification. The iris in front of the illumination objective, which had an adjustable aperture, was responsible for controlling the light-sheet characteristics.

The sCMOS high-speed scientific camera captured raw laser speckle images, while the CMOS camera was used to collect wide-field transmission images. Both cameras were triggered with the NI DAQ card for synchronized image acquisition, while their frame rates and exposure times were set independently in the LABView-based software designed for image acquisition and system control. For LSH-DSI imaging, the sCMOS frame rate determined the upper bound of the blood flow velocity to be measured. Therefore, faster blood flow often requires higher frame rates. On the other hand, an excessively high acquisition frame rate was avoided, as it caused an unnecessary strain on the system resources and slowed down the post-processing process.

4.3 LSH-DSI Image Processing

A raw LSH-DSI image stack typically consists of a few hundred to a few thousand 2D-intensity images. The dynamic changes in light intensity were analyzed pixel by pixel in MATLAB. Details of the processing method are illustrated in Fig. 4. Figure 4(a) shows a representative segment of the raw speckle signal. It was picked from a single pixel in a vein region, and its intensity fluctuated with time-dependent patterns. The signal was sampled at 3000 Hz for 2 s and was loaded into MATLAB as a 6000-element vector. A time-frequency analysis function "pspectrum" was used to compute short-time power spectrum estimates of the signal. The analysis result was a 2D matrix that represented the time-dependent signal spectra. As shown in Fig. 4(b), each column of the matrix was a short-time spectrum for one of 128 time points within the 2-s time. The frequency range for each spectrum was 1500 Hz, half of the sampling frequency. An alternative way to look at the spectra for all time points was to plot them as one-dimensional functions of frequency [Fig. 4(c)]. For most spectral lines, the power densities leveled off in the frequency range from 500 to 1500 Hz, indicating a noise floor of around 47.6 dB. In the frequency band below 500 Hz, the signal spectrum typically contained two distinctive lobes. The main lobe was close to direct current, which resulted from random interferences from microscopic scatterers. The sidelobe, indicated by the green arrow, was related to more periodic intensity fluctuations that involved both moving scatterers and stationary vascular structures.[57] In this work, we simply used the sidelobe information to quantify the flow velocities. To properly identify the sidelobes, we first set a power threshold to suppress noises. The effect of thresholding was apparent when we displayed the spectra in a power density range of 50 to 90 dB [Fig. 4(d)]. The background

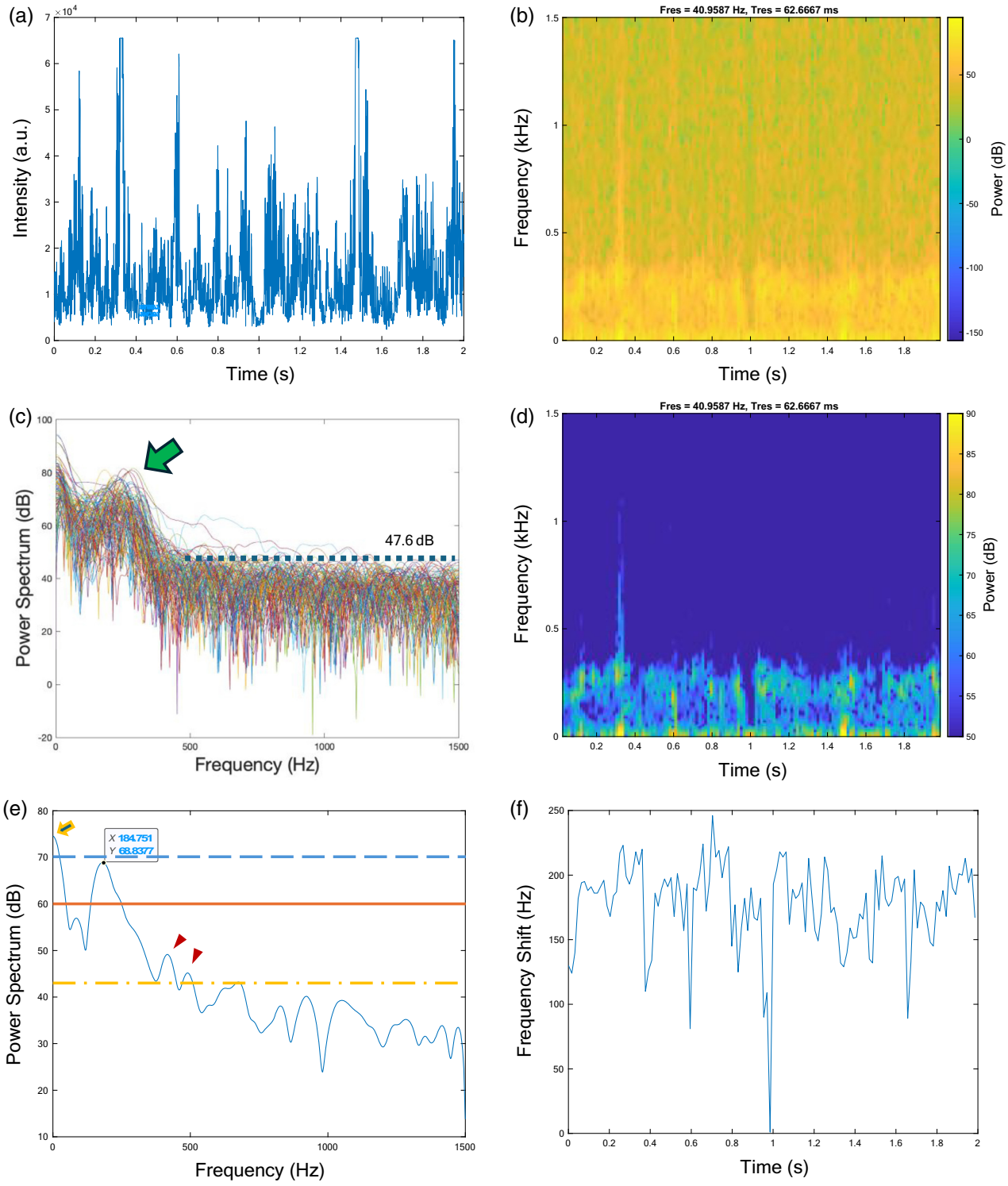

Fig. 4 Time-frequency analysis of speckle signals. (a) A segment of representative raw speckle signal that lasted for 2 s and was sampled at 3000 Hz. (b) The time-dependent power spectra of the signal in (a), displayed as a 2D function of time and frequency. (c) The family of time-dependent power spectra for all time points plotted as one-dimensional functions of frequency. (d) The same 2D spectra as in (b) displayed between 50 and 90 dB in power. (e) A sample power spectrum at one of the time points. Red line, a typical threshold at 60 dB for noise suppression and peak identification. The data tip indicates an identified spectral peak with a corresponding peak frequency shift (184.751 Hz) and peak power (68.8377 dB). Orange dashed-dotted line, a too-low threshold; blue dashed line, a too-high threshold. Dark red triangles, spurious peaks. Yellow arrow, low-frequency intensity fluctuation peak. (f) The peak frequency shifts for all time points in the 2-s window.

became clean, and the envelope of the peak frequency shifts could be better identified, as the lower bound of 50 dB was 2.4 dB above the noise floor. In this study, a typical threshold of around 60 dB was chosen. The peak frequency shift at each time point was found by searching the local peaks above the threshold in the corresponding spectrum. The data tip in Fig. 4(e) indicated a readily identified local peak with the maximum peak frequency shift. The peak power at this frequency was significantly higher than the threshold (red horizontal line). The orange (dashed-dotted) and blue (dashed) lines were included to illustrate hypothetical scenarios in which thresholds mismatched signal/noise levels. For instance, the orange threshold was comparable to the noise floor, and some spurious peaks (dark red arrows) would appear in the searching range and led to overestimated flow velocities. In another case, the signal peak power could fall below a too-high threshold (blue) and the peak frequency would not be included in the searching range. Consequently, the estimated flow velocities could be significantly lower than the true values. Therefore, it was apparent that an adequately high signal-to-noise ratio was essential to achieve high accuracy in flow velocity quantification. The peak frequency shifts were estimated point by point; the result is plotted in Fig. 4(f).

The local flow velocity is simply converted from the frequency shift f_0 by

$$v = \frac{\lambda f_0}{n \cos \theta}, \tag{2}$$

where θ is the angle between the illumination beam propagation direction and the flow (vessel) orientation.

4.4 PIVlab Image Processing

PIVlab is a graphic user interface-based MATLAB program designed for particle image velocimetry. We have used this software to process both transmission images and scalar velocity maps retrieved from laser speckle images.

The image processing procedures are as follows: First, an input image stack is imported into PIVlab. Second, one of the built-in algorithms is chosen for cross-correlation analysis. Usually, direct Fourier transform correlation with multiple passes and deforming windows (FFT window deformation) is preferred over single-pass direct cross-correlation and ensemble correlation. Third, the selected analysis is configured and performed, after which the results are calibrated using a calibration image acquired separately. Eventually, the velocity distributions in the FOV and instant velocity waveforms in specific regions of interest are generated. As an option, the blood vessel network can also be delineated by further processing the velocity maps.

5 Appendix B: Video Files

Video 1: A fly-through animation showing the captured zebrafish larvae head vasculature within a depth range of 300 μm (AVI, 3.9 MB).

Video 2: 3D rendering of zebrafish larvae head vasculature rotation along the y axis (AVI, 1.2 MB [URL: https://doi.org/10.1117/1.APN.4.1.016002.s2).

Disclosures

The authors declare that they have no competing interests.

Code and Data Availability

All data in support of the findings of this paper are available from the corresponding author upon reasonable request.

Acknowledgments

This work was supported by the following funding sources:
Ministry of Education – Singapore MOE2019-T2-2-094
Ministry of Education – Singapore Tier I R-397-000-327-114
Science and Technology Project of Jiangsu Province (Grant No. BZ2022056)
Biomedical and Health Technology Platform, National University of Singapore (Suzhou) Research Institute.

Author's Contributions

Conceptualization: N.C. Methodology: N.C., K.L., K.V.R., S.S., E.D., and Z.R. Investigation: K.L. and N.C. Supervision: N.C. and Z.G. Writing: N.C. and K.L.

References

1. O. Mennes et al., "Assessment of microcirculation in the diabetic foot with laser speckle contrast imaging," *Physiol. Meas.* **40**(6), 065002 (2019).
2. J. Yan et al., "*In vivo* label-free quantification of liver microcirculation using dual-modality microscopy," *J. Biomed. Opt.* **19**(11), 116006 (2014).
3. C. Sturesson et al., "Laser speckle contrast imaging for assessment of liver microcirculation," *Microvasc. Res.* **87**, 34–40 (2013).
4. E. Du et al., "Confocal laser speckle autocorrelation imaging of dynamic flow in microvasculature," *Opto-Electron. Adv.* **5**(2), 210045 (2022).
5. O. Genzel-Boroviczény, F. Christ, and V. Glas, "Blood transfusion increases functional capillary density in the skin of anemic preterm infants," *Pediatr. Res.* **56**(5), 751–755 (2004).
6. C. F. van Dijke et al., "Mammary carcinoma model: correlation of macromolecular contrast-enhanced MR imaging characterizations of tumor microvasculature and histologic capillary density," *Radiology* **198**(3), 813–818 (1996).
7. Y. Y. Foo et al., "4D modelling of fluid mechanics in the zebrafish embryonic heart," *Biomech. Model. Mechanobiol.* **19**, 221–232 (2020).
8. P. W. Elbers et al., "Microcirculatory imaging in cardiac anesthesia: ketanserin reduces blood pressure but not perfused capillary density," *J. Cardiothorac. Vasc. Anesth.* **23**(1), 95–101 (2009).
9. E. Klijn et al., "The heterogeneity of the microcirculation in critical illness," *Clin. Chest Med.* **29**(4), 643–654 (2008).
10. J. Zhou et al., "Angiography derived assessment of the coronary microcirculation: is it ready for prime time?" *Expert Rev. Cardiovasc. Ther.* **20**(7), 549–566 (2022).
11. E. Jonathan, J. Enfield, and M. J. Leahy, "Correlation mapping method for generating microcirculation morphology from optical coherence tomography (OCT) intensity images," *J. Biophotonics* **4**(9), 583–587 (2011).
12. X. Wang et al., "Noninvasive laser-induced photoacoustic tomography for structural and functional in vivo imaging of the brain," *Nat. Biotechnol.* **21**(7), 803–806 (2003).
13. R. Bonner and R. Nossal, "Model for laser Doppler measurements of blood flow in tissue," *Appl. Opt.* **20**(12), 2097–2107 (1981).
14. K. Wardell, A. Jakobsson, and G. E. Nilsson, "Laser Doppler perfusion imaging by dynamic light scattering," *IEEE Trans. Biomed. Eng.* **40**(4), 309–316 (1993).

15. G. E. Nilsson, T. Tenland, and P. A. Oberg, "Evaluation of a laser Doppler flowmeter for measurement of tissue blood flow," *IEEE Trans. Biomed. Eng.* **27**(10), 597–604 (1980).
16. P. A. Oberg, "Laser-Doppler flowmetry," *Crit. Rev. Biomed. Eng.* **18**(2), 125–163 (1990).
17. J. D. Briers, "Laser Doppler, speckle and related techniques for blood perfusion mapping and imaging," *Physiol. Meas.* **22**(4), R35 (2001).
18. Y. Tomita et al., "Long-term *in vivo* investigation of mouse cerebral microcirculation by fluorescence confocal microscopy in the area of focal ischemia," *J. Cereb. Blood Flow Metab* **25**(7), 858–867 (2005).
19. U. H. Von Andrian, "Intravital microscopy of the peripheral lymph node microcirculation in mice," *Microcirculation* **3**(3), 287–300 (1996).
20. Z. Al-Qazwini et al., "Ultrahigh-speed line-scan SD-OCT for four-dimensional *in vivo* imaging of small animal models," *Biomed. Opt. Express* **9**(3), 1216–1228 (2018).
21. M. Li et al., "Retinal microvascular network and microcirculation assessments in high myopia," *Am. J. Ophthalmol.* **174**, 56–67 (2017).
22. G. M. Richter et al., "Structural and functional associations of macular microcirculation in the ganglion cell-inner plexiform layer in glaucoma using optical coherence tomography angiography," *J. Glaucoma* **27**(3), 281 (2018).
23. V. X. Yang et al., "Endoscopic Doppler optical coherence tomography in the human gi tract: Initial experience," *Gastrointest. Endosc.* **61**(7), 879–890 (2005).
24. S. Mirg et al., "Photoacoustic imaging for microcirculation," *Microcirculation* **29**(6-7), e12776 (2022).
25. W.-Y. Tsai et al., "Photoacoustic and absorption spectroscopy imaging analysis of human blood," *PLos One* **18**(8), e0289704 (2023).
26. A. Taruttis and V. Ntziachristos, "Advances in real-time multispectral optoacoustic imaging and its applications," *Nat. Photonics* **9**(4), 219–227 (2015).
27. X. Zhang et al., "Optical and photoacoustic imaging *in vivo*: opportunities and challenges," *Chem. Biomed. Imaging* **1**(2), 99–109 (2023).
28. C. To et al., "Intraoperative tissue perfusion measurement by laser speckle imaging: a potential aid for reducing postoperative complications in free flap breast reconstruction," *Plast. Reconstr. Surg.* **143**(2), 287e–292e (2019).
29. W. Heeman et al., "Clinical applications of laser speckle contrast imaging: a review," *J. Biomed. Opt.* **24**(8), 080901 (2019).
30. B. Choi et al., "The role of laser speckle imaging in port-wine stain research: recent advances and opportunities," *IEEE J. Sel. Top. Quantum Electron.* **22**(3), 307–318 (2015).
31. S. S. Kazmi et al., "Expanding applications, accuracy, and interpretation of laser speckle contrast imaging of cerebral blood flow," *J. Cereb. Blood Flow Metab.* **35**(7), 1076–1084 (2015).
32. M. Nagahara et al., "*In vivo* measurement of blood velocity in human major retinal vessels using the laser speckle method," *Invest. Ophthalmol. Vis. Sci.* **52**(1), 87–92 (2011).
33. D. A. Boas and A. K. Dunn, "Laser speckle contrast imaging in biomedical optics," *J. Biomed. Opt.* **15**(1), 011109 (2010).
34. P. Zakharov et al., "Dynamic laser speckle imaging of cerebral blood flow," *Opt. Express* **17**(16), 13904–13917 (2009).
35. H. Cheng, Y. Yan, and T. Q. Duong, "Temporal statistical analysis of laser speckle images and its application to retinal blood-flow imaging," *Opt. Express* **16**(14), 10214–10219 (2008).
36. P. Zakharov et al., "Quantitative modeling of laser speckle imaging," *Opt. Lett.* **31**(23), 3465–3467 (2006).
37. J. D. Briers and S. Webster, "Laser speckle contrast analysis (LASCA): a nonscanning, full-field technique for monitoring capillary blood flow," *J. Biomed. Opt.* **1**(2), 174–179 (1996).
38. H. Fujii, "Visualisation of retinal blood flow by laser speckle flowgraphy," *Med. Biol. Eng. Comput.* **32**, 302–304 (1994).
39. J. Briers and A. Fercher, "Retinal blood flow visualization by means of laser speckle," in *Opt. Biomed. Sci.: Proc. Int. Conf.*, Graz, Austria, September 7–11, 1981 pp. 158–161 (1982).
40. E. Du et al., "Depth-dependent microscopic flow imaging with line scan laser speckle acquisition and analysis," in *Optics in Health Care and Biomedical Optics XI*, pp. 20–26 (2021).
41. E. Du et al., "Multifunctional laser speckle imaging," *Biomed. Opt. Express* **11**(4), 2007–2016 (2020).
42. W. Heeman et al., "Application of laser speckle contrast imaging in laparoscopic surgery," *Biomed. Opt. Express* **10**(4), 2010–2019 (2019).
43. P. G. Vaz et al., "Laser speckle imaging to monitor microvascular blood flow: a review," *IEEE Rev. Biomed. Eng.* **9**, 106–120 (2016).
44. T. Iwase et al., "Differences of retinal blood flow between arteries and veins determined by laser speckle flowgraphy in healthy subjects," *Medicine (Baltimore)* **94**(33) (2015).
45. T. Sugiyama, "Basic technology and clinical applications of the updated model of laser speckle flowgraphy to ocular diseases," *Photonics* **1**, 220–234 (2014).
46. B. Ruaro et al., "Laser speckle contrast analysis: a new method to evaluate peripheral blood perfusion in systemic sclerosis patients," *Ann. Rheum. Dis.* **73**(6), 1181–1185 (2014).
47. B. Manwani et al., "Perfusion of ischemic brain in young and aged animals: a laser speckle flowmetry study," *Stroke* **45**(2), 571–578 (2014).
48. H. Li et al., "Directly measuring absolute flow speed by frequency-domain laser speckle imaging," *Opt. Express* **22**(17), 21079–21087 (2014).
49. J. Huisken and D. Y. Stainier, "Selective plane illumination microscopy techniques in developmental biology," *Development* **136**(12), 1963–1975 (2009).
50. H. Jia et al., "Axial resolution enhancement of light-sheet microscopy by double scanning of Bessel beam and its complementary beam," *J. Biophotonics* **12**(1), e201800094 (2019).
51. C. Liu et al., "Extended field of view of light-sheet fluorescence microscopy by scanning multiple focus-shifted Gaussian beam arrays," *Opt. Express* **29**(4), 6158–6168 (2021).
52. S. Gu et al., "Multiple airy beams light-sheet fluorescence microscopy," *Front. Phys.* **10**, 1111023 (2022).
53. D. Di Battista et al., "Enhanced light sheet elastic scattering microscopy by using a supercontinuum laser," *Methods Protoc.* **2**(3), 57 (2019).
54. Z. Yang et al., "Light sheet tomography (LST) for *in situ* imaging of plant roots," *Opt. Express* **21**(14), 16239–16247 (2013).
55. M. Diouf et al., "Demonstration of speckle resistance using space–time light sheets," *Sci. Rep.* **12**(1), 14064 (2022).
56. J. Kim, "Recent advances in oblique plane microscopy," *Nanophotonics* **12**(13), 2317–2334 (2023).
57. K. Long et al., "Light-sheet laser speckle imaging," *PREPRINT (Version 1) Available at Research Square* (2022).

Kai Long is a PhD student in the Department of Biomedical Engineering, National University of Singapore (NUS). Currently, his research interest is light-sheet microscopy. He is passionate about the development of advanced optical microscopy platforms and bioimaging applications.

Nanguang Chen is currently an associate professor of biomedical engineering at the NUS. His research interest is biomedical optical imaging, including diffuse optical tomography, optical coherence tomography, and novel microscopy.

Biographies of the other authors are not available.